

University of Dundee

256 × 2 SPAD line sensor for time resolved fluorescence spectroscopy

Krstajić, Nikola; Levitt, James; Poland, Simon; Ameer-Beg, Simon; Henderson, Robert K

Published in:
Optics Express

DOI:
[10.1364/OE.23.005653](https://doi.org/10.1364/OE.23.005653)

Publication date:
2015

Document Version
Publisher's PDF, also known as Version of record

[Link to publication in Discovery Research Portal](#)

Citation for published version (APA):

Krstajić, N., Levitt, J., Poland, S., Ameer-Beg, S., & Henderson, R. K. (2015). 256 × 2 SPAD line sensor for time resolved fluorescence spectroscopy. *Optics Express*, 23(5), 5653-69. <https://doi.org/10.1364/OE.23.005653>

General rights

Copyright and moral rights for the publications made accessible in Discovery Research Portal are retained by the authors and/or other copyright owners and it is a condition of accessing publications that users recognise and abide by the legal requirements associated with these rights.

- Users may download and print one copy of any publication from Discovery Research Portal for the purpose of private study or research.
- You may not further distribute the material or use it for any profit-making activity or commercial gain.
- You may freely distribute the URL identifying the publication in the public portal.

Take down policy

If you believe that this document breaches copyright please contact us providing details, and we will remove access to the work immediately and investigate your claim.

256 × 2 SPAD line sensor for time resolved fluorescence spectroscopy

Nikola Krstajić,^{1,2,4} James Levitt,³ Simon Poland,³ Simon Ameer-Beg,³
and Robert Henderson^{1,*}

¹Institute for Integrated Micro and Nano Systems, School of Engineering, University of Edinburgh, Edinburgh, UK

²EPSRC IRC “Hub” in Optical Molecular Sensing & Imaging, Centre for Inflammation Research, Queen's Medical Research Institute, 47 Little France Crescent, University of Edinburgh, Edinburgh, UK

³Division of Cancer Research & Randall Division of Cell and Molecular Biophysics, Richard Dumbleby Department of Cancer Research, Guy's Campus, Kings College, London, UK

⁴n.krstajic@physics.org

^{*}robert.henderson@ed.ac.uk

Abstract: We present a CMOS chip 256 × 2 single photon avalanche diode (SPAD) line sensor, 23.78 μm pitch, 43.7% fill factor, custom designed for time resolved emission spectroscopy (TRES). Integrating time-to-digital converters (TDCs) implement on-chip mono-exponential fluorescence lifetime pre-calculation allowing timing of 65k photons/pixel at 200 Hz line rate at 40 ps resolution using centre-of-mass method (CMM). Per pixel time-correlated single-photon counting (TCSPC) histograms can also be generated with 320 ps bin resolution. We characterize performance in terms of dark count rate, instrument response function and lifetime uniformity for a set of fluorophores with lifetimes ranging from 4 ns to 6 ns. Lastly, we present fluorescence lifetime spectra of multicolor microspheres and skin autofluorescence acquired using a custom built spectrometer. In TCSPC mode, time-resolved spectra are acquired within 5 minutes whilst in CMM mode spectral lifetime signatures are acquired within 2 ms for fluorophore in cuvette and 200 ms for skin autofluorescence. We demonstrate CMOS line sensors to be a versatile tool for time-resolved fluorescence spectroscopy by providing parallelized and flexible spectral detection of fluorescence decay.

©2015 Optical Society of America

OCIS codes: (040.1240) Arrays; (040.5160) Photodetectors; (040.3780) Low light level; (300.2530) Fluorescence, laser-induced; (300.6500) Spectroscopy, time-resolved; (170.6280) Spectroscopy, fluorescence and luminescence.

References and links

1. J. R. Lakowicz, *Principles of Fluorescence Spectroscopy*, 3rd edition (Springer, 2010).
2. J. A. Levitt, D. R. Matthews, S. M. Ameer-Beg, and K. Suhling, “Fluorescence lifetime and polarization-resolved imaging in cell biology,” *Curr. Opin. Biotechnol.* **20**(1), 28–36 (2009).
3. G. O. Fruhwirth, L. P. Fernandes, G. Weitsman, G. Patel, M. Kelleher, K. Lawler, A. Brock, S. P. Poland, D. R. Matthews, G. Kéri, P. R. Barber, B. Vojnovic, S. M. Ameer-Beg, A. C. C. Coolen, F. Fraternali, and T. Ng, “How Förster Resonance Energy Transfer Imaging Improves the Understanding of Protein Interaction Networks in Cancer Biology,” *ChemPhysChem* **12**(3), 442–461 (2011).
4. W. Becker, *Advanced Time-Correlated Single Photon Counting Techniques*, (Springer, 2005).
5. G.-F. Dalla Betta, L. Panzeri, D. Stoppa, R. Henderson, and J. Richardson, “Avalanche Photodiodes in Submicron CMOS Technologies for High-Sensitivity Imaging,” in *Advances in Photodiodes*, G.-F. Dalla Betta, ed. (InTech, 2011).
6. E. Charbon, M. Fishburn, R. Walker, R. K. Henderson, and C. Niclass, “SPAD-Based Sensors,” in *TOF Range-Imaging Cameras*, F. Remondino and D. Stoppa, eds. (Springer Berlin Heidelberg, 2013), pp. 11–38.
7. E. Charbon, “Single-photon imaging in complementary metal oxide semiconductor processes,” *Philosophical Transactions of the Royal Society of London A: Mathematical Physical and Engineering Sciences* **372**(2012), 20130100 (2014).
8. S. Cova, M. Ghioni, A. Lotito, I. Rech, and F. Zappa, “Evolution and prospects for single-photon avalanche diodes and quenching circuits,” *J. Mod. Opt.* **51**(9-10), 1267–1288 (2004).
9. S. Cova, A. Longoni, and A. Andreoni, “Towards picosecond resolution with single photon avalanche diodes,” *Rev. Sci. Instrum.* **52**(3), 408–412 (1981).

10. A. Tosi, A. D. Mora, F. Zappa, and S. Cova, "Single-photon avalanche diodes for the near-infrared range: detector and circuit issues," *J. Mod. Opt.* **56**(2-3), 299–308 (2009).
11. J. Richardson, E. A. G. Webster, L. A. Grant, and R. K. Henderson, "Scaleable Single-Photon Avalanche Diode Structures in Nanometer CMOS Technology," *IEEE Trans. Electron. Dev.* **58**(7), 2028–2035 (2011).
12. J. Richardson, R. Walker, L. Grant, D. Stoppa, F. Borghetti, E. Charbon, M. Gersbach, and R. K. Henderson, "A 32 x32 50ps resolution 10 bit time to digital converter array in 130nm CMOS for time correlated imaging," in *IEEE Custom Integrated Circuits Conference, 2009. CICC '09* (2009), pp. 77–80.
13. C. Veerappan, J. Richardson, R. Walker, D.-U. Li, M. W. Fishburn, Y. Maruyama, D. Stoppa, F. Borghetti, M. Gersbach, R. K. Henderson, and E. Charbon, "A 160 x128 single-photon image sensor with on-pixel 55ps 10b time-to-digital converter," in *Solid-State Circuits Conference Digest of Technical Papers (ISSCC), 2011 IEEE International* (2011), pp. 312–314.
14. S. P. Poland, N. Krstajić, S. Coelho, D. Tyndall, R. J. Walker, V. Devaughes, P. E. Morton, N. S. Nicholas, J. Richardson, D. D.-U. Li, K. Suhling, C. M. Wells, M. Parsons, R. K. Henderson, and S. M. Ameer-Beg, "Time-resolved multifocal multiphoton microscope for high speed FRET imaging in vivo," *Opt. Lett.* **39**(20), 6013–6016 (2014).
15. W. Becker, A. Bergmann, and C. Biskup, "Multispectral fluorescence lifetime imaging by TCSPC," *Microsc. Res. Tech.* **70**(5), 403–409 (2007).
16. Q. S. Hanley, "Spectrally resolved fluorescent lifetime imaging," *J. R. Soc. Interface* **6**(Suppl_1), S83–S92 (2009).
17. L. Brand and J. R. Gohlke, "Nanosecond Time-resolved Fluorescence Spectra of a Protein-Dye Complex," *J. Biol. Chem.* **246**(7), 2317–2319 (1971).
18. J. H. Easter, R. P. DeToma, and L. Brand, "Nanosecond time-resolved emission spectroscopy of a fluorescence probe adsorbed to L-alpha-egg lecithin vesicles," *Biophys. J.* **16**(6), 571–583 (1976).
19. M. G. Badea, R. P. DeToma, and L. Brand, "Nanosecond relaxation processes in liposomes," *Biophys. J.* **24**(1), 197–212 (1978).
20. J. R. Lakowicz, E. Gratton, H. Cherek, B. P. Maliwal, and G. Laczo, "Determination of time-resolved fluorescence emission spectra and anisotropies of a fluorophore-protein complex using frequency-domain phase-modulation fluorometry," *J. Biol. Chem.* **259**(17), 10967–10972 (1984).
21. S. Coda, A. J. Thompson, G. T. Kennedy, K. L. Roche, L. Ayaru, D. S. Bansi, G. W. Stamp, A. V. Thillainayagam, P. M. W. French, and C. Dunsby, "Fluorescence lifetime spectroscopy of tissue autofluorescence in normal and diseased colon measured ex vivo using a fiber-optic probe," *Biomed. Opt. Express* **5**(2), 515–538 (2014).
22. Y. Sun, R. Liu, D. S. Elson, C. W. Hollars, J. A. Jo, J. Park, Y. Sun, and L. Marcu, "Simultaneous time- and wavelength-resolved fluorescence spectroscopy for near real-time tissue diagnosis," *Opt. Lett.* **33**(6), 630–632 (2008).
23. D. R. Yankelevich, D. Ma, J. Liu, Y. Sun, Y. Sun, J. Bec, D. S. Elson, and L. Marcu, "Design and evaluation of a device for fast multispectral time-resolved fluorescence spectroscopy and imaging," *Rev. Sci. Instrum.* **85**(3), 034303 (2014).
24. A. Rück, Ch. Hülshoff, I. Kinzler, W. Becker, and R. Steiner, "SLIM: A new method for molecular imaging," *Microsc. Res. Tech.* **70**(5), 485–492 (2007).
25. F. V. Bright and C. A. Munson, "Time-resolved fluorescence spectroscopy for illuminating complex systems," *Anal. Chim. Acta* **500**(1-2), 71–104 (2003).
26. D. Tyndall, B. Rae, D. Li, J. Richardson, J. Arlt, and R. Henderson, "A 100Mphoton/s time-resolved mini-silicon photomultiplier with on-chip fluorescence lifetime estimation in 0.13 um CMOS imaging technology," in *Solid-State Circuits Conference Digest of Technical Papers (ISSCC)* (2012), pp. 122–124.
27. I. Nissinen, J. Nissinen, A.-K. Lansman, L. Hallman, A. Kilpela, J. Kostamovaara, M. Kogler, M. Aikio, and J. Tenhunen, "A sub-ns time-gated CMOS single photon avalanche diode detector for Raman spectroscopy," in *Solid-State Device Research Conference (ESSDERC)* (2011), pp. 375–378.
28. J. Blacksberg, Y. Maruyama, E. Charbon, and G. R. Rossman, "Fast single-photon avalanche diode arrays for laser Raman spectroscopy," *Opt. Lett.* **36**(18), 3672–3674 (2011).
29. J. Kostamovaara, J. Tenhunen, M. Kögler, I. Nissinen, J. Nissinen, and P. Keränen, "Fluorescence suppression in Raman spectroscopy using a time-gated CMOS SPAD," *Opt. Express* **21**(25), 31632–31645 (2013).
30. Y. Maruyama, J. Blacksberg, and E. Charbon, "A 1024 x 8, 700-ps Time-Gated SPAD Line Sensor for Planetary Surface Exploration With Laser Raman Spectroscopy and LIBS," *IEEE J. Solid-State Circuits* **49**(1), 179–189 (2014).
31. Z. Li and M. J. Deen, "Towards a portable Raman spectrometer using a concave grating and a time-gated CMOS SPAD," *Opt. Express* **22**(15), 18736–18747 (2014).
32. S.-S. Kiwanuka, T. K. Laurila, J. H. Frank, A. Esposito, K. Blomberg von der Geest, L. Pancheri, D. Stoppa, and C. F. Kaminski, "Development of Broadband Cavity Ring-Down Spectroscopy for Biomedical Diagnostics of Liquid Analytes," *Anal. Chem.* **84**(13), 5489–5493 (2012).
33. R. M. Rich, M. Mummert, Z. Gryczynski, J. Borejdo, T. J. Sørensen, B. W. Laursen, Z. Foldes-Papp, I. Gryczynski, and R. Fudala, "Elimination of autofluorescence in fluorescence correlation spectroscopy using the AzaDiOxaTriAngulenium (ADOTA) fluorophore in combination with time-correlated single-photon counting (TCSPC)," *Anal. Bioanal. Chem.* **405**(14), 4887–4894 (2013).
34. R. Richards-Kortum and E. Sevick-Muraca, "Quantitative Optical Spectroscopy for Tissue Diagnosis," *Annu. Rev. Phys. Chem.* **47**(1), 555–606 (1996).

35. E. A. G. Webster, J. A. Richardson, L. A. Grant, D. Renshaw, and R. K. Henderson, "A Single-Photon Avalanche Diode in 90-nm CMOS Imaging Technology With 44% Photon Detection Efficiency at 690 nm," *IEEE Electron Device Lett.* **33**(5), 694–696 (2012).
36. E. A. G. Webster, L. A. Grant, and R. K. Henderson, "A High-Performance Single-Photon Avalanche Diode in 130-nm CMOS Imaging Technology," *IEEE Electron Device Lett.* **33**(11), 1589–1591 (2012).
37. D. D.-U. Li, J. Arlt, D. Tyndall, R. Walker, J. Richardson, D. Stoppa, E. Charbon, and R. K. Henderson, "Video-rate fluorescence lifetime imaging camera with CMOS single-photon avalanche diode arrays and high-speed imaging algorithm," *J. Biomed. Opt.* **16**(9), 096012 (2011).
38. N. Krstajić, S. Poland, D. Tyndall, R. Walker, S. Coelho, D. D. Li, J. Richardson, S. Ameer-Beg, and R. Henderson, "Improving TCSPC data acquisition from CMOS SPAD arrays," in (2013), Vol. 8797, pp. 879709–879709–8.
39. D.-U. Li, B. Rae, R. Andrews, J. Arlt, and R. Henderson, "Hardware implementation algorithm and error analysis of high-speed fluorescence lifetime sensing systems using center-of-mass method," *J. Biomed. Opt.* **15**(1), 017006 (2010).
40. M. Wahl, T. Röhlicke, H.-J. Rahn, R. Erdmann, G. Kell, A. Ahlrichs, M. Kernbach, A. W. Schell, and O. Benson, "Integrated multichannel photon timing instrument with very short dead time and high throughput," *Rev. Sci. Instrum.* **84**(4), 043102 (2013).
41. J. L. Rinnenthal, C. Börnchen, H. Radbruch, V. Andresen, A. Mossakowski, V. Siffrin, T. Seelemann, H. Spiecker, I. Moll, J. Herz, A. E. Hauser, F. Zipp, M. J. Behne, and R. Niesner, "Parallelized TCSPC for Dynamic Intravital Fluorescence Lifetime Imaging: Quantifying Neuronal Dysfunction in Neuroinflammation," *PLoS ONE* **8**(4), e60100 (2013).
42. H. M. Shapiro, *Practical Flow Cytometry* (John Wiley & Sons, 2005).
43. J. Richardson, L. A. Grant, and R. K. Henderson, "Low Dark Count Single-Photon Avalanche Diode Structure Compatible With Standard Nanometer Scale CMOS Technology," *IEEE Photon. Technol. Lett.* **21**(14), 1020–1022 (2009).
44. D. Tyndall, B. R. Rae, D. D.-U. Li, J. Arlt, A. Johnston, J. A. Richardson, and R. K. Henderson, "A High-Throughput Time-Resolved Mini-Silicon Photomultiplier With Embedded Fluorescence Lifetime Estimation in 0.13 μm CMOS," *IEEE Trans Biomed Circuits Syst* **6**(6), 562–570 (2012).
45. N. Krstajić, R. Hogg, and S. J. Matcher, "Common path Fourier domain optical coherence tomography based on multiple reflections within the sample arm," *Opt. Commun.* **284**(12), 3168–3172 (2011).
46. N. Krstajić, C. T. A. Brown, K. Dholakia, and M. E. Giardini, "Tissue surface as the reference arm in Fourier domain optical coherence tomography," *J. Biomed. Opt.* **17**(7), 071305 (2012).
47. Z. Bay, "Calculation of Decay Times from Coincidence Experiments," *Phys. Rev.* **77**(3), 419 (1950).
48. I. Isenberg and R. D. Dyson, "The Analysis of Fluorescence Decay by a Method of Moments," *Biophys. J.* **9**(11), 1337–1350 (1969).
49. S. Preus, K. Kilså, F.-A. Miannay, B. Albinsson, and L. M. Wilhelmsson, "FRETmatrix: a general methodology for the simulation and analysis of FRET in nucleic acids," *Nucleic Acids Res.* **2012**, gks856 (2012).
50. S. Preus, "DecayFit - Fluorescence Decay Analysis Software 1.3, FluorTools, www.fluortools.com," (2014).
51. M. G. Badea and L. Brand, "[17] Time-resolved fluorescence measurements," in *Methods in Enzymology*, S. N. T. C.H.W. Hirs, ed., Enzyme Structure Part H (Academic Press, 1979), Vol. Volume 61, pp. 378–425.
52. European Machine Vision Association, "EMVA Standard 1288 - Standard for Characterization of Image Sensors and Cameras Release 3.0," (2010).
53. L. Liu, J. Qu, Z. Lin, L. Wang, Z. Fu, B. Guo, and H. Niu, "Simultaneous time- and spectrum-resolved multifocal multiphoton microscopy," *Appl. Phys. B* **84**(3), 379–383 (2006).
54. J. Blackwell, K. M. Katika, L. Pilon, K. M. Dipple, S. R. Levin, and A. Nouvong, "In vivo time-resolved autofluorescence measurements to test for glycation of human skin," *J. Biomed. Opt.* **13**(1), 014004 (2008).
55. K. C. B. Lee, J. Siegel, S. E. D. Webb, S. Lévesque-Fort, M. J. Cole, R. Jones, K. Dowling, M. J. Lever, and P. M. W. French, "Application of the Stretched Exponential Function to Fluorescence Lifetime Imaging," *Biophys. J.* **81**(3), 1265–1274 (2001).
56. L. Marcu, "Fluorescence Lifetime Techniques in Medical Applications," *Ann. Biomed. Eng.* **40**(2), 304–331 (2012).
57. A. Gibson and H. Dehghani, "Diffuse optical imaging," *Philos Trans A Math Phys Eng Sci* **367**(1900), 3055–3072 (2009).

1. Introduction

Fluorescence spectroscopy is an essential tool in microscopy, biomedicine and biotechnology [1]. This is due to the fact that fluorescence contains important molecular information and the instrumentation is becoming increasingly cost-effective. Most current fluorescence spectroscopy is performed in steady-state mode, i.e. by integrating spectra from a constant output light source. While one can exploit steady-state fluorescence intensity, polarization and spectroscopy in a relatively straightforward fashion, one key aspect of fluorescence is the decay constant (fluorescence lifetime) or the average time needed for molecule to go from excited to ground state. Shifts in the fluorescence lifetime indicate changes in the surrounding environment [2]. For example, Förster resonance energy transfer (FRET) is one of many

mechanisms that can be inferred from fluorescence lifetime changes and is of increasing importance in studying the complex network of protein-protein interactions [3]. Time-correlated single photon counting (TCSPC) has been the preferred method for accurate lifetime measurement [4]. Whilst TCSPC has the advantage of detecting full fluorescence decay as a histogram of photon arrival times, it is usually slower due to constraints imposed by pile-up artefacts whereby photon arrival rate should be limited to 1% of the pulsed laser repetition rate (for a discussion on pile-up see section 7.9 in [4]).

The work presented here is part of a larger effort to design and apply multichannel TCSPC systems by designing custom analogue application-specific integrated circuits (ASICs) with combined light sensitive and timing circuitry [5–7]. The light sensitive element is a single photon avalanche diode (SPAD) which is an avalanche photodiode biased beyond breakdown for single photon sensitivity. Time resolved SPAD structures with picosecond performance have a long history [8]. The common approach has been to deploy custom and high voltage complementary metal-oxide semiconductor structures (HV-CMOS) [9] covering visible and near-infrared [10]. Standard CMOS promises low power implementation of scalable, massively parallel multi-channel TCSPC, albeit limited to the visible range [11–13].

Advances in integrated SPAD sensor arrays promise much faster acquisition of fluorescence lifetime data in live cell imaging [14]. Spectroscopy is particularly attractive as time-resolved emission (fluorescence) spectroscopy (TRES) contains multi-dimensional information across temporal and spectral axes which can be used to derive spectral relaxation properties and fluorescence lifetimes, see chapter 7 in [1] and [15,16]. TRES has a long history and the first systems were implemented in 1970's, for example see [17–19]. These systems relied on 10 kHz flashlamp with associated cuvette readout, monochromator and multi-channel analyzer (MCA). The main interest has been in using TRES for better understanding of solvation dynamics and excited state reactions. This work was followed up by frequency domain TRES [20]. In recent years the applications range from studying endogenous fluorescence lifetime in tissues [21–23], molecular imaging [24], and analytical chemistry [25]. Since its inception TRES has been limited by the complexity of optical and electronics instrumentation involved. We believe the results presented in this paper show significant advance in TRES performance and simplicity which has been achieved by adopting scalable CMOS SPAD arrays.

The geometry of line sensors allows for high fill-factor SPAD designs and further innovations in time resolution and noise performance. The high data rates limiting larger TCSPC cameras are not applicable to spectroscopy applications which usually do not need more than several thousand pixels. It is also possible to transfer methods (e.g. related pile-up immunity [26]) from silicon photomultiplier (SiPM) architectures to line arrays. Recent work has shown promising results in time-resolved Raman spectroscopy [27–31] opening up the possibility to remove fluorescence background by time gating only the Raman signal coincidental to laser pulse. CMOS SPAD arrays have also been used in sensitive absorbance measurements [32]. Similar ideas can be explored in removal of autofluorescence [33] since the lifetime associated with endogenous fluorophores is often shorter than exogenous fluorophores [34].

We present a SPAD line array manufactured in a 130 nm CMOS process. The sensor has 2 line arrays, each with 256 pixels. The first array is optimized for detection of wavelength range 450 nm to 550 nm (henceforth referred to as blue SPAD line array) and the second array optimized for 600 nm to 900 nm (henceforth referred to as red SPAD line array) [35,36]. Due to higher photon detection efficiency and lower noise of the red compared with the blue SPAD line array, this paper focuses on the red SPAD line array. We present the spectrometer SPAD array architecture and performance regarding time resolution, noise, instrument response function (IRF) uniformity and fluorescence lifetime uniformity.

Two features distinguish this chip from prior work [27–31]. Firstly, all 256 pixels have individual TCSPC circuitry. Even though the pixel number is less than in related work (for example [30]), we believe highly parallelized TCSPC is a powerful tool in low light circumstances. It can act as both a measurement tool for fluorescence decays and time gating

can be done by post-processing the acquired TCSPC histograms. Secondly, the spectrometer SPAD array has computational logic to calculate the “center of mass” (CMM) of photon arrival times on the fly. This dramatically improves photon efficiency as it removes the need to transfer TDC codes from the SPAD array to surrounding circuitry. For example, whilst each SPAD can detect up to 30 million photon arrival codes per second (assuming ~ 33 ns dead-time), the number of events that can actually be transmitted (for the whole SPAD array) is limited, for example, to 20-40 million codes per second for universal serial bus version 2 (USB2) (assuming 2 bytes per code). Even taking into account pile-up and inherently low photon budget in many specimens, for a 100MHz repetition rate laser, one should be able to acquire 1 million photon arrival codes per second per SPAD. CMM allows millions of codes to be compressed to 1000 [37] or less depending on photon count rate and any scanning arrangements [38]. Previously, we implemented CMM on field programmable gate arrays (FPGAs) and 1000 photon arrival codes were enough to estimate lifetime [37,39]. The CMM calculation depended on the available throughput between the camera and the FPGA and not on the SPAD. One of our aims in this paper is to demonstrate that each photon can contribute to lifetime calculation using on-chip calculation on the CMOS SPAD array without resorting to FPGA resources.

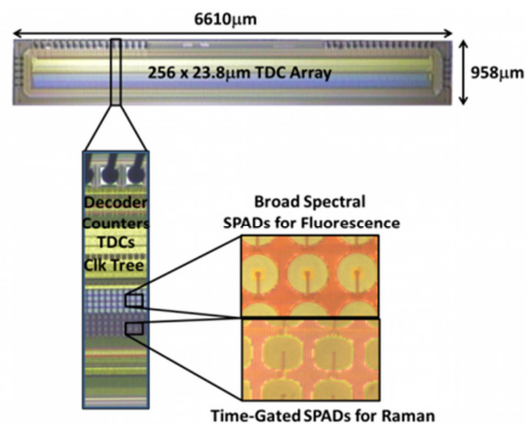


Fig. 1. Spectrometer chip micrograph.

Commercial TCSPC systems usually have optimal count rates from SPADs or photomultiplier tubes (PMTs), but they are mostly single channel systems. Recently 8 channel [40] and 16 channel [41] TCSPC systems have been introduced. In the case of 16 channel system [41] the channels are not truly independent at high count rates due to the high probability of co-incidence or cross-talk. Although limited to mono-exponential lifetime estimation, the on-chip CMM approach we have implemented here opens up possibilities for applications where photon budget is high, for example in flow cytometry [42].

2. Chip architecture

A micrograph of the line sensor detailing the main blocks is shown in Fig. 1. The $6610 \mu\text{m} \times 958 \mu\text{m}$ sensor is integrated in a 130 nm CMOS image sensor technology. It comprises three main subsystems; a 256×2 SPAD array and front-end electronics, time-gate generation and clock distribution electronics and a TDC array, addressing and data readout system. Pixel data is read out via a serial interface operating at 8 MHz, as 43-bit words providing 200 spectra per second.

2.1 SPAD array

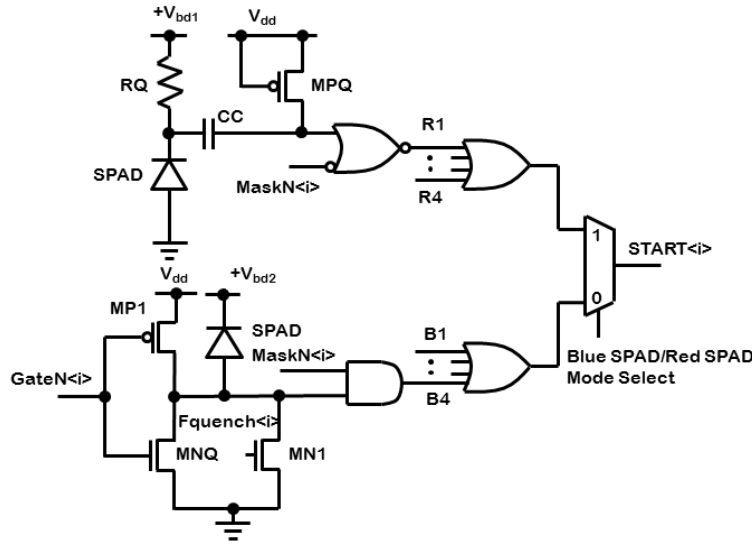


Fig. 2. SPADs and interface circuitry. Multiplexer selects between blue SPAD (bottom, B1 to B4) and red SPAD (top R1 to R4). Red SPAD can be masked while blue SPAD can be time gated.

Four wide spectral range SPAD detectors (R1 to R4 in Fig. 2 top) [36] employing a circular deep-n-well to p-substrate active region with $18.2\ \mu\text{m}$ diameter are arranged in a $100\ \mu\text{m}$ column, $23.8\ \mu\text{m}$ pixel width. Fill factor of four circular areas $18.2\ \mu\text{m}$ in diameter is 43.7% of the total $23.8 \times 100\ \mu\text{m}$ available for the pixel. These detectors are interfaced to low voltage digital electronics via a $400\ \text{k}\Omega$ polysilicon resistor and a $10\ \text{fF}$ metal-oxide-metal finger capacitor (Fig. 2 top). An off-PMOS transistor (MPQ) maintains a high state through leakage current at the input of a NOR-gate allowing the SPAD output pulses to be masked. This detector cannot easily be gated off because gating transistors tolerant of high voltages at the SPAD anode are not available. However, this is not an impediment as this detector is used for fluorescence lifetime detection where gating is unnecessary.

A second set of four SPADs employing a shallow p-well to deep-n-well active region is also implemented (B1 to B4 Fig. 2 bottom) [43]. These devices are drawn as square with rounded (super-ellipse) corners and a diameter of $16\ \mu\text{m}$. The deep-n-well cathode is shared between devices to increase the fill-factor to 43.7%. In this case, the cathode of the device can be rapidly raised and lowered around breakdown voltage to time-gate the SPAD off or on by means of conventional low-voltage MOS transistors. The GateN signal deactivates the SPAD via a PMOS transistor (MP1) and re-enables it via the Fquench signal and NMOS transistor MN1. A long NMOS MNQ provides a passive quench resistance. During the interval that the GateN signal inhibits the SPAD, a signal MaskN prevents the high state from triggering the TDC falsely. This timing is assured by a per-pixel circuit receiving three delayed waveforms P1, P2 and P3 from the on-chip timing generator (Fig. 3).

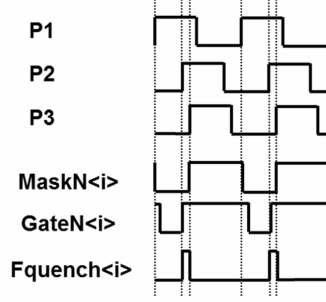


Fig. 3. SPAD gating waveforms.

2.2 Time-gate generation

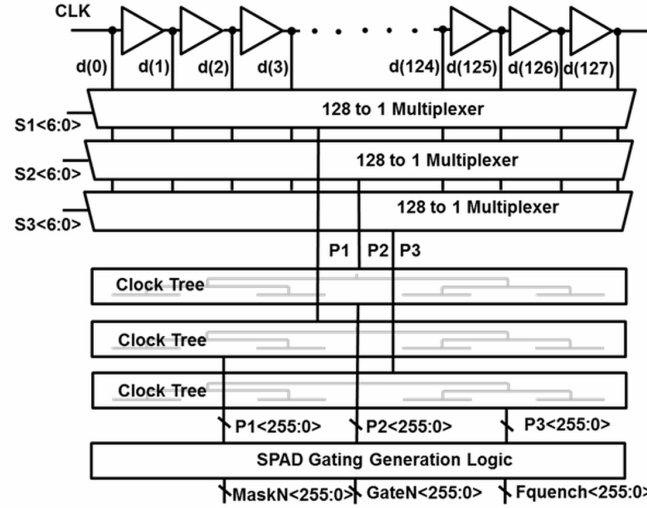


Fig. 4. Gate timing generator.

An on-chip digital to time converter (Fig. 4) generates three programmable delayed versions of an input clock waveform (typically derived from a laser sync signal). A delay line is composed of 128 current-starved buffer cells with unit delays of 850 ps. Three 128 to 1 multiplexers select a single tapped delayed version of the input clock to generate P1, P2 and P3. These delayed clocks pass through clock trees to the pixel gating logic to ensure synchronized behaviour of all detectors in the array.

2.3 Integrating Time to Digital Converter

For a fluorescence histogram with a single-exponential decay $f(t) = A \exp(-t/\tau)$ in a measurement window $0 \leq t \leq T$ its centre of mass (CM) is approximated to the lifetime τ . Where a TDC quantizes the measurement window into M time bins with the bin width of h a further approximation is possible:

$$\tau_{CMM} = \frac{\int_0^T t f(t) dt}{\int_0^T f(t) dt} \cong \frac{\sum_{j=0}^{M-1} j N_j}{N_c} h. \quad (1)$$

where N_j is the number of recorded counts in the j^{th} time bin ($j = 0, 1, \dots, M-1$), and N_C is the total signal count within the measurement window. The lifetime τ can therefore be calculated as the summation of TDC time stamps divided by the number of detected photons. CMM has previously been implemented as an embedded algorithm on the FPGA and in an ASIC [39,44].

We propose a TDC circuit which *inherently* implements the CMM method (Fig. 5). A 3.1 GHz, 4-stage differential ring oscillator with reset signal R and start signal S drives a coarse 27 bit counter. The circuit operates in reverse start-stop method, meaning that a SPAD event starts the ring oscillator which is stopped on the following rising edge of the laser sync clock (Fig. 6). The ring oscillator holds its internal state and resumes from this condition on each subsequent photon detection, effectively integrating the total sequence of time intervals through the action of the counter.

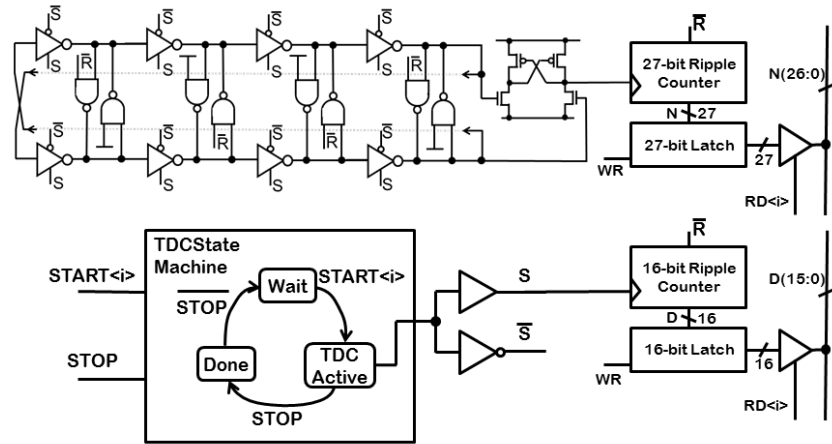


Fig. 5. Integrating time to digital converter.

A 16-bit counter counts the number of detected photons forming the denominator of the CMM formula. The maximal rate of 65k photons in the 2 ms line time equates to the maximum SPAD frequency of around 30 MHz limited by dead time of SPAD. At the end of an exposure period, the numerator N and denominator D words are transferred to registers by pulsing the write signal WR. An address decoder allows random access readout of specific TDC values at wavelengths of interest through tri-state buffers onto a shared output bus. The TDC is then reset by pulsing R, clearing the counters and initializing the ring oscillator.

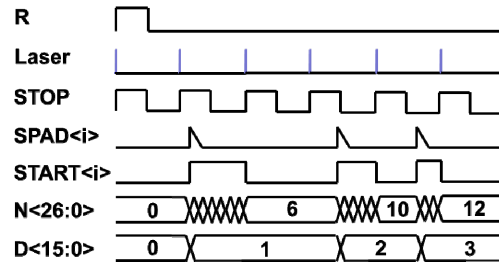


Fig. 6. Integrating TDC timing.

3. Materials and methods

3.1 Optical testing configurations

Two opto-electronic arrangements for the line sensor were built to test for timing uniformity (Fig. 7(a)) and spectral lifetime (Fig. 7(b)). Fluorescent dye solution was placed in a cuvette and illuminated by a pulsed laser diode. Throughout this study we use three pulsed laser diodes: Picoquant 485 nm laser diode head, Hamamatsu 443 nm laser and Hamamatsu 654 nm laser. Illumination at 443 nm and 654 nm was used to estimate the IRF variability with illumination wavelength. This is important as broadband spectral decay data sets will need to take into account any “colour effects” (see section 4.6.5 in [1]). The pulsed laser has an electrical synchronization trigger BNC cable connected to the line sensor PCB (not shown). Laser repetition rates used were 10 MHz and 20 MHz. To test timing uniformity across the line sensor, the cuvette was illuminated by pulsed laser and detected at 90° with fluorescence emission focused onto the line sensor via a lens and a 500 nm long pass filter (Thorlabs FEL0500) as shown on Fig. 7(a). IRFs were acquired by placing a scattering (Ludox) solution in the quartz cuvette (10 mm pathlength) and detecting the scattered signal without the long pass filter.

Time resolution of the pixels was determined using BNC cables of two different lengths (1 m and 2 m) and observing the shift in IRF position on the TCSPC histogram. The velocity factor of the BNC cable was 0.66, so the 5.05 ns shift in the IRF was measurable accurately. The repetition rate of the laser was 10 MHz and we ensured scattered light had a spot size larger than detector.”

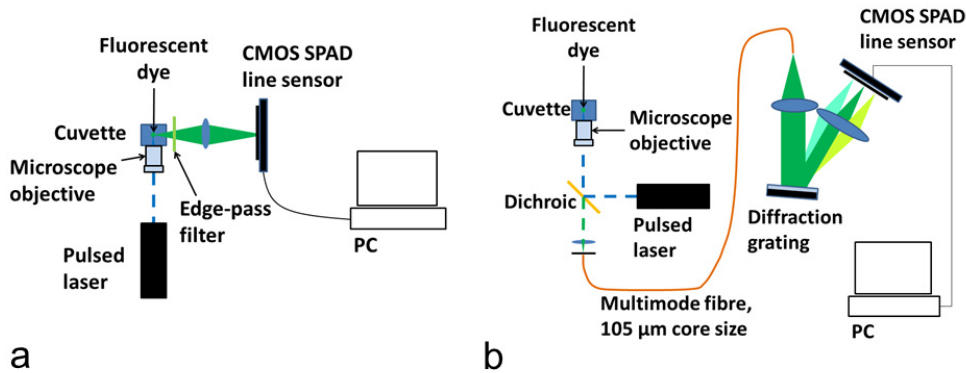


Fig. 7. Line sensor fluorescence test setups comprising cuvette readout for uniformity tests (a) and custom-built spectrometer linked to cuvette via multimode fiber and epifluorescence readout (b).

The spectral lifetime arrangement was operated in epi-fluorescence mode. The illumination and collection optic was an infinity corrected $\times 10$, NA 0.25 microscope objective (Olympus Plan Achromat Objective). A dichroic beamsplitter (Thorlabs DMLP505) separates the fluorescence light which in turn was focused onto a 105 μm multimode fibre (MMF) (Thorlabs M43L01). A long pass filter is also present further filtering fluorescence above 500 nm. Fluorescence coupled into the MMF was dispersed in a custom spectrometer comprising of a ruled reflection grating (1200 grooves per mm, blaze wavelength 500 nm, Thorlabs GR25-1205) and focusing optics similar to that presented before [45,46]. The spectra were calibrated to cover 500 nm to 600 nm over 256 pixels. This was verified by comparing spectra from the spectrometer chip with spectra obtained from an off-the-shelf spectrometer (USB2000 Ocean Optics). To perform this comparison, the multimode fibre shown in Fig. 7(b) can alternatively be connected to a separate spectrometer. The efficiency of the spectrometer over the wavelength range is $\sim 70\%$ as measured by optical power meter.

Spectral resolution was ~ 1.2 nm due to the slit size (105 μm). The line sensor is controlled via custom FPGA firmware and PC software written in Labview 2011 (National Instruments, Texas, USA) for flexible operation in a variety of modes (TCSPC, time-gated and CMM). In this manuscript we focus on TCSPC and CMM aspects of the sensor.

3.2 TCSPC and CMM

The main aim of work presented is to demonstrate prompt spectral lifetime data acquisition using novel CMOS SPAD arrays. Two methods have been used to provide fluorescence lifetime, namely CMM and TCPSC.

Prior work on CMM incorporates FIRST and LAST settings [37,39] which provide the boundaries for the histogram window. This is useful since the center of mass for the decay curve is required and not necessarily the whole of the histogram. On-chip implementation of the CMM, however, does not include FIRST and LAST settings due to circuit complexity involved for the current spectrometer chip revision. Therefore, the CMM was estimated by first acquiring CMM of the IRF and then acquiring the CMM of the decay. The difference between the two values is indicative of changes in lifetime and this we call CMM_{diff} in the present article [47,48]. Longer lifetimes will stretch the decay curve further away from the IRF. A unique feature of this detector is that each photon acquired is automatically used to estimate lifetime. Whilst not quantitative, this value is of interest when lifetimes are compared rather than measured accurately. Exact validity of subtracting CMM of decay from CMM of IRF is not the topic of this manuscript and will be addressed in future work. CMM_{diff} values were obtained with the following exposure times: 2 ms, 200 ms and 2 s to cross compare the noise on spectral CMM_{diff} .

Spectral TCSPC was acquired in 5 minutes. For uniformity, test acquisition times were longer in order to test the chip performance. As mentioned before, laser triggering is provided by the laser diode and the spectrometer chip works in reverse START-STOP mode. Decays were fitted using a customized version of DecayFit software [49,50]. Solutions of fluorescein and 1,8 – anilinonaphthalenesulphonate (ANS) were used to verify measurements of TCSPC and CMM_{diff} uniformity. Multi-color constellation microspheres (Life Technologies, part number C-14837) were used to demonstrate different spectral lifetimes.

TRES was derived by scaling wavelength-dependent decay curves so that the sum along the time axes were equal to steady state spectra of the same sample (see section 7.2.2 in [1] and [51] for details). Steady state spectra for TRES scaling were acquired using a USB2000 spectrometer (Ocean Optics, USA). The main reason for doing this was to compensate for photon response non uniformity (PRNU) which was measured to be 20%. PRNU measurements were done using an established standard [52].

4. Results

4.1 Dark count rate (DCR)

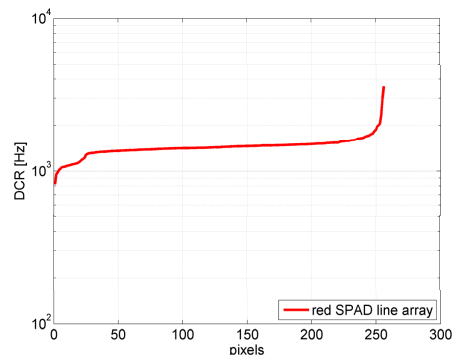


Fig. 8. DCR of the red SPAD line array.

Dark count rate (DCR) plot for red SPAD line array at room temperature (25 C°) is shown in Fig. 8. Median DCR for SPAD array is 1.4 kHz.

4.2 Time resolution

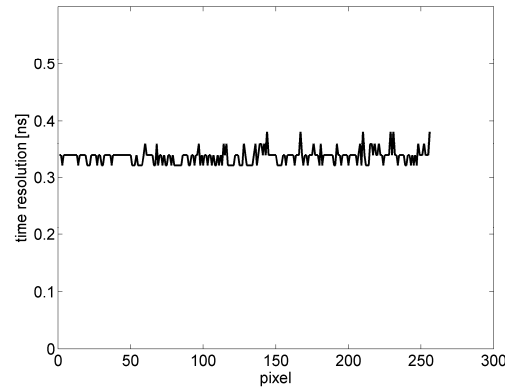


Fig. 9. Time resolution across the 256 pixels of the line sensor.

Time resolution spread across chip is shown on Fig. 9. As the number of TCSPC channels is high (256 or one timing channel per pixel), the variability of time resolution across the array needs to be taken into account in order to reduce errors in decay estimates. Throughout this study we assume mean time resolution of 320 ps.

4.3 IRF

Figure 10(a) shows an IRF from one pixel whilst Fig. 10(b) shows the variation of IRF FWHM across the chip at high illumination (close to saturation and with a lot of SPAD activity – 5 MHz per pixel) and low illumination (50 kHz per pixel). Both measurements were undertaken using a 443 nm laser diode. Jitter performance is significantly worse towards the middle of the array at high illumination where it reaches 0.9 ns. At high illumination all TDCs work in parallel and highly correlated SPAD activity causes the droop in the power supply voltage across the array. This in turn modulates the time resolution affecting the jitter measurement. Under normal operation (less than 1 million counts per second per pixel) we obtain a uniform temporal resolution with FWHM of IRF ~ 0.7 ns as shown in low illumination curve in Fig. 10(b).

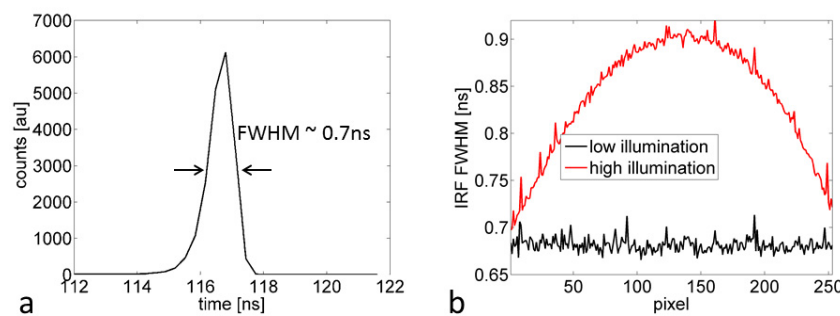


Fig. 10. (a) Sample IRF from one pixel, (b) IRF FWHM across chip.

Chromatic effect is investigated in Fig. 11. The red SPAD line array IRF FWHM at 443nm is higher by 165 ps than at 654 nm (Fig. 11(a)). The red SPAD line array IRF location variability is shown on Fig. 11(b). The standard deviation of IRF location variation is 1.05

time bins or 336 ps. Blue SPAD line array IRF FWHM does not change with wavelength (Fig. 11(c)) while the standard deviation of IRF location changes by 1.3 time bins or 416 ps. IRF location variability is due to droop in the power supply across the line array.

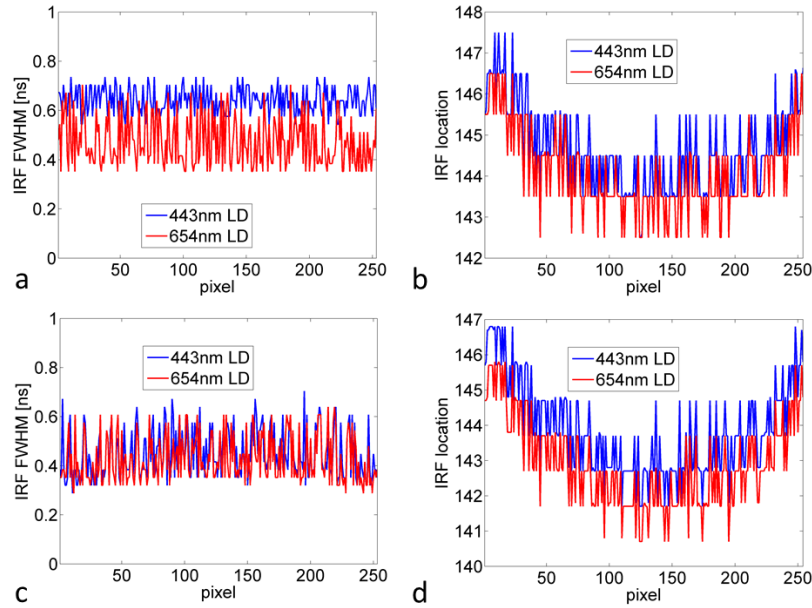


Fig. 11. (a) Red SPAD line array IRF FWHM at 443 nm and 654 nm, (b) red SPAD line array IRF location variability across chip, (c) blue SPAD line array IRF FWHM at 443 nm and 654 nm, (d) blue SPAD line array IRF location variability across chip (y axis units are in TDC bins).

4.4 Histogram artefacts

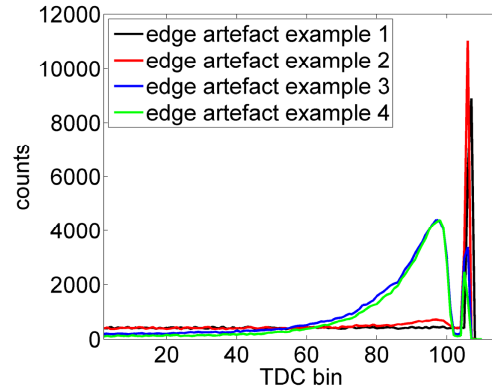


Fig. 12. Edge peaks on the right side of each plot have different peak values for the same experiment. Pixels 20, 60, 100 and 150 are plotted from the same experiment where spectral decay was measured.

TCSPC is subject to many measurement artefacts and care needs to be taken to minimize stray light reaching the detector and to reduce scattering of the sample. Characterization of the spectrometer chip revealed an artefact related to the chip rather than the setup. Noisier pixels or pixels under more intense illumination produce a strong artefactual signal at early times (right hand side) of the reverse START-STOP histogram (i.e. close to laser sync START), as

shown in Fig. 12. For example, the green curve in Fig. 12 decays to values close to 0 at TDC bins 0 to 20. It also has the lowest edge artefact. This indicates that pixel's DCR and ambient scattering will deteriorate the CMM measurement. The main cause for this artifact is in level sensitive logic in the TDC triggering. This allows SPADs to fire during the TDC dead time and create an instant event on TDC re-enabling. Revised chip design will remove this artefact.

Whilst TCSPC mode of operation is not affected by this, CMM mode is. This is simply due to the varying “weight” imposed by the edge artefact. In CMM mode, the spectrometer chip does not acquire a histogram, but sums all photon arrival times and divides by the number of photons. This compresses the histogram to one number from which the edge peak is hard to extract and correct. As the peak height increases with total signal, this moves the centre-of-mass towards the peak which is not desired since it contains no information. As the peak varies in amplitude for IRF, sample and across the array, calibration for CMM is more complex, but with workarounds is perfectly feasible. For example, by reducing the laser repetition rate and attenuating light, representative CMM_{diff} values can be obtained, provided the specimen does not scatter significantly.

4.5 Fluorescence lifetime TCSPC mode and CMM mode

Figure 13 shows fluorescein decay in TCSPC mode. The acquisition time was set to 60 minutes to gather enough counts for sensor characterization.

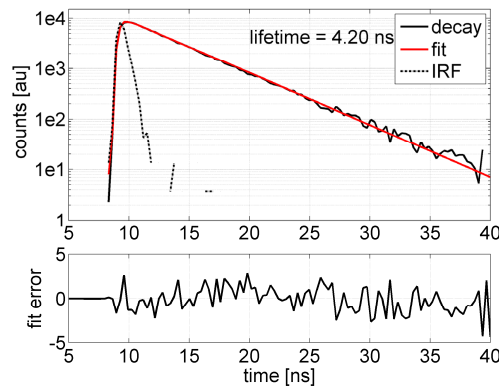


Fig. 13. Sample decay, fluorescein.

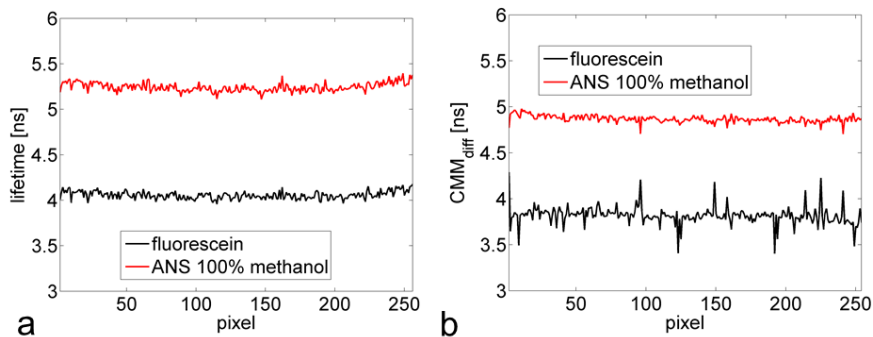


Fig. 14. TCSPC mode results for two fluorophores (a) and CMM mode (b).

Fluorescein and ANS lifetime calculations in TCSPC and CMM modes are shown in Fig. 14. Acquisition time in TCSPC mode took 60 minutes (250 photon counts per second), whilst the CMM mode took 2 minutes (~10000 photon counts per second). Lifetime values are as

expected from prior work [39] and the lifetime uniformity across the chip does not show significant systematic variations.

4.6 Time resolved emission spectroscopy

The main aim of the present work is to illustrate TRES applications of the CMOS SPAD line array. Below we present results of experiments from cuvette fluorescence readouts using the arrangement given in Fig. 7(b). Whilst the chip can have excellent performance when tested alone, we extensively tested the chip in a variety of time resolved fluorescence spectroscopy scenarios.

4.6.1 Spectral CMM_{diff}

The fastest way of obtaining a lifetime estimate from the spectrometer chip is to exploit its capability to integrate TDC time-stamps whilst recording total photon counts. The ratio of the two provides an average time-stamp and, in ideal conditions, the number represents the centre-of-mass of the decay curve (see section 2C).

Figure 15(a) shows spectral CMM_{diff} of multicolor microspheres while Fig. 15(b) shows spectral CMM_{diff} of skin autofluorescence. Within 2 ms a fast estimate of spectral fluorescence lifetime can be achieved in cuvette conditions, while skin autofluorescence spectra can be obtained within 200 ms. The noise on the curve is predominantly shot noise as the value is derived from an average ~ 200 photons/pixel. 200 ms and 2s spectral CMM_{diff} curves contain on average 20000 and 200000 photons/pixel respectively and are consequently lower noise. Assuming fluorescence is almost saturating the pixel, the dead time is 33 ns and the CMM_{diff} can be obtained from 1000 photons then the minimum time to acquire a CMM_{diff} value would be 33 μs .

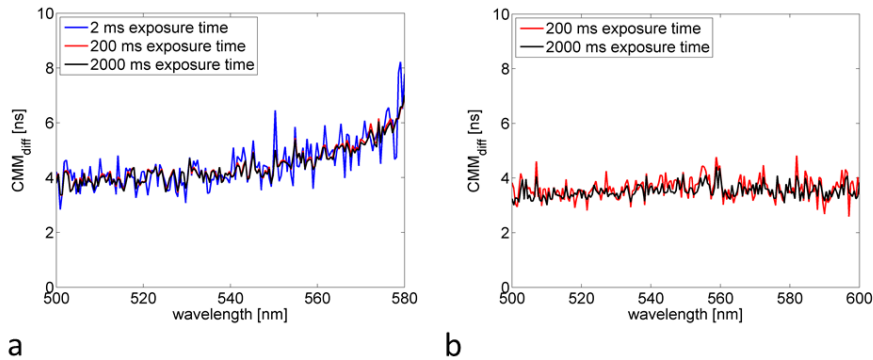


Fig. 15. (a) Spectral CMM_{diff} for 2 ms, 200 ms and 2 s exposure times of colour microspheres. As expected, the increased exposure time reduces the noise. (b) Spectral CMM_{diff} for 200 ms and 2 s exposure times of skin autofluorescence.

We illustrate this below in Fig. 16(a) where fast acquisition of IRF (via scattered light from Ludox) shows CMM to be uniform even for mean flux of 100 photons/ pixel (200 μs exposure time). In this case, we did not subtract two CMM values as the reference 0 value is a prior measurement of IRF over 50 ms exposure time. We disregard potential pile-up effects in this instance, because we aim to demonstrate photon capture capability of the spectrometer chip. In normal fluorescence lifetime experiments the effects of scatter, pile-up and other artefacts need to be carefully considered before performing an experiment.

Figure 16(b) illustrates the variation of error on CMM estimates across the line sensor. 256 plots of changes in standard deviation of CMM estimates for 50 readings are plotted with increasing exposure time from 200 μs to 2 ms. Standard deviation reduces from 150 ps to about 60 ps (center of the envelope). The least desirable scenario is 300 ps for 200 μs exposure time reducing to 140 ps for 2 ms exposure time.

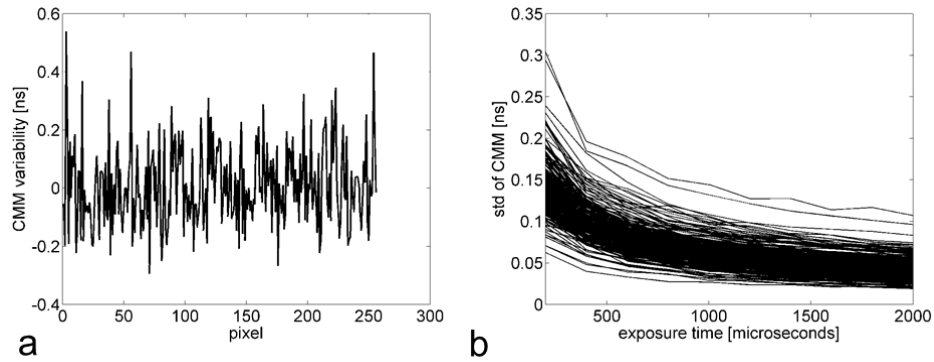


Fig. 16. (a) CMM for 200 μ s and 2 ms exposure times. Mean photon count per pixel was 100 photons for 200 μ s exposure time. (b) Standard deviation of CMM value obtained for 50 repeated measurements of IRF with exposure times ranging from 200 μ s to 2 ms. 256 curves are plotted to illustrate the spread of CMM variation across all pixels.

4.6.2 Spectral TCSPC

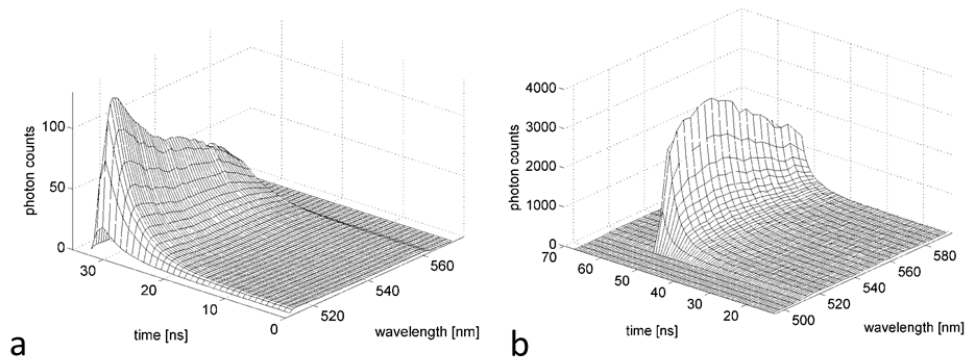


Fig. 17. (a) 3D spectral decay plot for multicolour microspheres, (b) skin autofluorescence. For display purposes every 3rd decay is shown. A moving average of 7 pixels was used to smooth the spectrum display in order to remove the effect of ~ 10 noisy pixels.

TRES decays were obtained for multi-colour microspheres (Fig. 17(a)) and skin autofluorescence (Fig. 17(b)). The total acquisition time was 5 minutes. The spectral decays were acquired in parallel, thereby demonstrating the advantage of having TCSPC units working for each pixel.

From time-resolved spectral decays one can obtain lifetime for each wavelength, but also spectral relaxation curves. For example, the 3D decay plot of multicolor microspheres in Fig. 17(a) can be formatted to show spectral relaxation curves (see Fig. 18(a)) while lifetime vs wavelength is shown in Fig. 18(b). The observed increase in lifetime corresponds to prior observations [53]. Similarly, the 3D decay plot of skin autofluorescence is formatted to show spectral relaxation curves in Fig. 18(c) and spectral lifetime in Fig. 18(d). Although the fluorescence lifetime does not change with wavelength in the case of skin autofluorescence, the chi square error indicates that the analysis should be multiexponential rather than single exponential, as presented here.

This is illustrated in Fig. 19, where a sample decay curve is shown for skin autofluorescence at 530 nm. The decay is obviously not a single exponential decay, but a more complex one, as would be expected from skin. Tri-exponential fit is applied and the

values broadly correspond to those published previously [54]. However, the multiexponential fits on complex heterogeneous tissue fluorescence need to be treated with caution [55] and more detailed study is needed. Fluorescence lifetime is becoming an increasingly accessible tool for clinical applications [56] and spectral lifetime provides an additional dimension to data acquired.

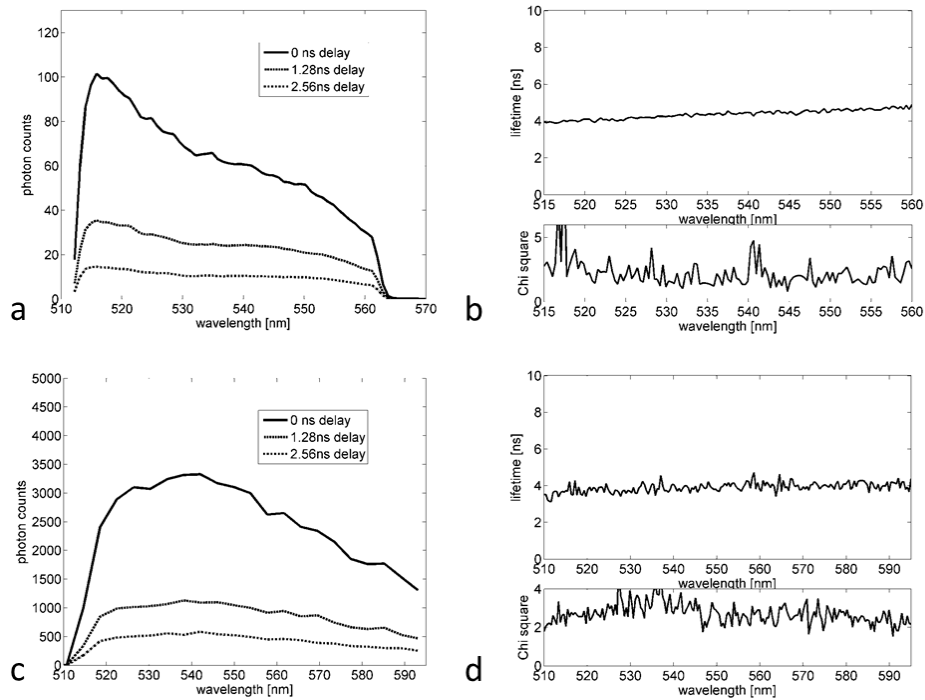


Fig. 18. (a) Spectral relaxation plots extracted from Fig. 17 (a) for multicolor microspheres. (b) Corresponding fluorescence lifetime increase with increasing wavelength for multicolor microspheres. (c) Spectral relaxation plots extracted from Fig. 17 (b) for skin autofluorescence. (d) Corresponding spectral fluorescence lifetime curve for skin autofluorescence.

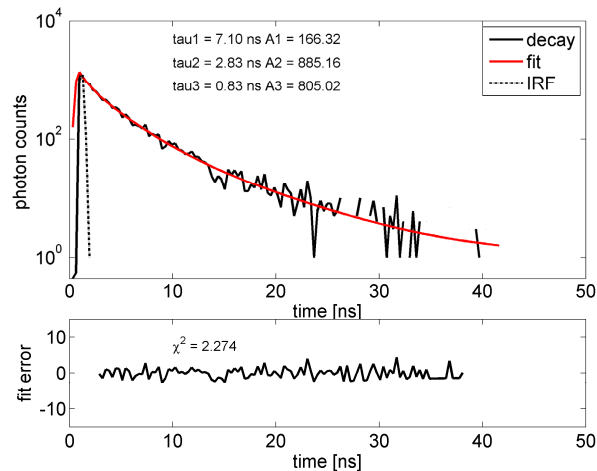


Fig. 19. Skin autofluorescence decay curve at 530 nm. Decay is not a simple single exponential as can be seen by curved decay on log scale plot.

5. Discussion

We presented a unique platform for time-resolved spectroscopy which can acquire full spectral decays in parallel and without resorting to monochromator or compromising with low spectral resolution. To the best of our knowledge this is the most parallelized time resolved spectrometer system to date with 256 TCSPC channels.

Some improvements are needed. The line rate from chip to PC is currently 200 spectra per second, which is low for TCSPC work in cell biology. However, for analyzing complex decays of fluorophores in solutions with cuvette readouts and time resolved tissue autofluorescence spectra, the photon budgets tend to be low. The PCB and chip architecture should allow an upgrade to 10-20 kHz line rate assuming USB2 data rates (30-40 MB/s). PRNU was measured to be 20% which is poor by today's standards, but this has not seriously affected TRES work as these were scaled by steady state spectra obtained with off-the-shelf spectrometer. More work is needed in calibrating pixels and verifying the underlying reasons for poor PRNU.

Time resolved spectroscopy is a broad field and fluorescence need not be the only application. Related biomedical fields exploiting backscattered light such as diffuse optical tomography (DOT) [57] and molecular fingerprint techniques such as Raman spectroscopy would all benefit from high-performance time resolved line sensors such as the one presented here. Low light sensitivity detection coupled with high time resolution lends these detectors to compact multimodal applications, especially considering the developments in pulsed lasers (both pulsed laser diodes and fiber lasers).

5. Conclusion

We have demonstrated multi-channel TCSPC line array of SPADs in fluorescence spectroscopy applications. We plan to apply the spectrometer chip and associated setups to measuring fluorescence kinetics of a variety of dyes and intrinsic fluorescence (autofluorescence) spectra of tissue. We believe line arrays of SPADs are an ideal test-bed for advanced scientific CMOS SPAD architectures. As time-resolution and noise performances are improved, more applications are likely to emerge across the boundaries of medicine, chemistry, biology and physics.

Acknowledgments

We would like to thank Biotechnology and Biological Sciences Research Council (BBSRC, United Kingdom) (grant numbers BB/I022937/1 and BB/I022074/1), Engineering and Physical Sciences Research Council (EPSRC, United Kingdom) Interdisciplinary Research Collaboration (grant number EP/K03197X/1) and the Medical Research Council (MRC, United Kingdom) (grant number MR/K015664/1) for funding this work. We would like to thank ST Microelectronics, Imaging Division, Edinburgh, for their generous support in manufacture of spectrometer SPAD array. We would also like to thank David Tyndall, Dialog Semiconductor, for providing support on spectrometer chip PCB design, David Li, University of Strathclyde, for suggesting CMM of IRF as a reference value for CMM estimates, Richard Walker, University of Edinburgh, for help with FPGA firmware, Dr Lina Imati, University of Edinburgh, for preparing ANS fluorescence dyes, Dr Mike Tanner, Heriot-Watt University, for numerous useful discussions.